Scaling laws for aerodynamic loads and acoustics of wall-mounted plates at different deflection angles

Owen Parnis [ID] *, David Angland [ID]

Faculty of Engineering and Physical Sciences, University of Southampton, Southampton, SO167QF, United Kingdom

ARTICLE INFO

ABSTRACT

Inclined flat plates mounted on horizontal surfaces have applications in the aerospace, renewable energy and automotive sectors. While previous studies have examined how aspect ratio and proximity to a mounting surface affect aerodynamic loads on a plate, a systematic investigation of scaling laws for aerodynamic loads and acoustics is lacking. This paper establishes scaling relationships for the aerodynamic loads and the flow-induced noise generated by a wall-mounted flat plate inclined to the flow. Wind tunnel experiments were conducted using a Kevlar-walled test section, with a wall-mounted flat plate deflected between 10° and 90° across various Reynolds numbers. A correction method based on the bluff body blockage corrections of Maskell and calibrated using open test section wind tunnel data is presented in this work to account for solid and wake blockage effects in the Kevlar test section experiments. For aerodynamic loads, the normalized normal force coefficient collapses when scaled with projected frontal area, converging to a fixed value of the drag coefficient at 90°. This provides a simple predictive methodology for the aerodynamic loads with maximum errors of $\Delta C_D = 0.073$ and $\Delta C_L = 0.081$. The scaling law presented in this work is unique for wall-mounted flat plates and differs for flat plates in freestream. Aeroacoustic analysis reveals broadband noise without coherent vortex shedding. The noise scales approximately, but not perfectly, with the sixth power of velocity. The slight variations in the value of the velocity exponent at different deflection angles highlight that it does not simply scale as a compact dipole but other effects are present, including non-compactness and edge scattering effects. The acoustic scaling with projected area exhibits different behaviour at low and high deflection angles. At low deflection angles, the plate is partially immersed in the boundary layer, reducing the acoustic intensity variation with deflection angle. At higher deflection angles (> 30°), the acoustic intensity scaled with the projected area to a power of 1.2 again indicating additional sources besides the scaling of pure compact dipole sources.

1. Introduction

Flat plates at different angles of incidence have been studied extensively in the field of aerodynamics to characterize two- and three-dimensional bodies (Wick, 1954; Abernathy, 1962; Chen and Feng, 1996; Taira and Colonius, 2009; Hemmati et al., 2018; Pieris et al., 2022). The aerodynamic performance of flat plates can be primarily determined by the angle of incidence (deflection), δ_{fp}, of the plate with respect to the freestream, which strongly influences the drag characteristics (Ortiz et al., 2015). At low incidence angles, the drag is dominated by the viscous forces, whereas at larger incidence angles, pressure drag becomes dominant. The transition between these two regimes is highly dependent on the plate's aspect ratio (AR) (Torres and Mueller, 2004) defined as the span-to-chord ratio of the plate (b/c).

Early work presented by Fage and Johansen (1927) on two-dimensional flat plates in freestream identified two regimes in the variation of the normal force coefficient, C_N, with incidence in the direction of the freestream velocity. At low incidence angles (< 9°), C_N increases rapidly. Above 9°, the rate of increase diminishes, reaching a plateau at high incidence angles (> 80°) corresponding to the drag coefficient of a plate normal to the flow.

Subsequent studies investigated the three-dimensional effects for flat plates up to an aspect ratio of 5 (Flachsbart, 1932; Holmes et al., 2005; Mizoguchi and Yamaguchi, 2012), highlighted that reducing the aspect ratios yields lower normal force coefficients, corresponding to a reduction in the drag coefficients, C_D, at large incidence angles. This three-dimensional effect stems from edge vortices originating along the spanwise edges of the plate. For low aspect ratios, these vortices extend towards the plate's mid-span section (Hoerner, 1965). The lower pressure along the downstream base region, compared to the freestream,

---

* Corresponding author.
  E-mail address: o.parnis@soton.ac.uk (O. Parnis).

induces inward flow deflection from the edges towards the centreline, resulting in increased average base pressure, C_{p_b}, near the edges.

Experimental research conducted for flat plates and cambered plane wings (Pelletier and Mueller, 2000; Torres and Mueller, 2004; Gutierrez-Castillo et al., 2021) up to an aspect ratio of 8 along the pre-stall region of the plate, highlighted an increase in the lift curve slope, with an increase in aspect ratio. The plates exhibited a more linear lift slope for $AR > 1.25$ as a result of a reduction in the influence of the induced velocity along the suction surfaces, generating additional lift as a result of the influence of the edge vortices. Gutierrez-Castillo et al. (2021) proposed a semi-empirical correlation for the prediction of the lift curve slope as a function of the aspect ratio and Reynolds number. The correlation is based on Prandtl's lifting line, but includes the influence of Reynolds number, and is capable of predicting lift up to pre-stall angles of incidence.

Recent studies have considered the influence of ground proximity on the aerodynamic load characteristics of inclined three-dimensional plates. Ortiz et al. (2015) and Pieris et al. (2022) highlighted that proximity effects are particularly pronounced near the angle corresponding to maximum lift. However, the sensitivity is highly dependent on the aspect ratio of the plate and the direction of plate deflection. Pieris et al. (2022) highlighted that ground proximity did not fundamentally change the loading trends with respect to the deflection angle compared to the freestream case. It was shown that plates having an aspect ratio of 2 and deflected in the direction of the freestream velocity vector showed negligible differences to the freestream results, irrespective of the proximity ratio between the leading edge of the plate and the ground.

In many practical applications, such as aircraft spoilers (Parnis and Angland, 2025), photovoltaic panels (Aly and Bitsuamlak, 2013; Strobel and Banks, 2014), and deflector plates on automobiles (Capone and Romano, 2019), plates are wall-mounted rather than in the freestream. Wall-mounted flat plate aerodynamics is more complex due to additional governing parameters, including the ratio of incoming boundary layer thickness to plate chord, δ/c, the plate deflection angle, δ_{fp}, the aspect ratio, AR, the yaw angle relative to freestream, ψ, and the clearance ratio defined as the height of the plate's leading edge above the mounted planar surface, g/c (Hoerner, 1965; Everitt, 1982; Ortiz et al., 2015; Montes Gomez and Sumner, 2022).

Parnis and Angland (2025) defined the flow topology around a wall-mounted inclined flat plate spoiler at a deflection angle of 30° using numerical simulations. The flow topology in terms of the Q-criterion iso-volume representation is shown in Fig. 1. The presence of the plate generates an adverse pressure gradient upstream, causing the incoming boundary layer to separate and form a horseshoe vortex structure that wraps around the inclined plate, moving downstream towards the trailing edge of the mounting plate. The strength of this horseshoe vortex depends on the deflection angle of the inclined plate. Additionally, two ground-edge vortices are generated from the side-edges of the inclined plate. These are located inboard of the horseshoe vortex and rotate in the opposite direction.

Acoustic scaling laws for wall-mounted bodies have mainly been developed for cylindrical and prismatic geometries (King and Pfizenmaier, 2009; Moreau and Doolan, 2013; Porteous et al., 2014; Wang et al., 2019). Building upon Curle's acoustic analogy (Curle, 1955), Phillips (1956) demonstrated for two-dimensional cylinders that the mean square acoustic pressure radiated by the body is predominantly governed by lift fluctuations and exhibits a U_∞^6 velocity scaling, characteristic of a dipole-like source. The scaling has been confirmed for both wall-mounted geometries, including cylinders (King and Pfizenmaier, 2009; Porteous et al., 2013) and prisms (Wang et al., 2019). Maruta and Kanagawa (1981) extended the analysis to the flow-induced noise of flat plates in freestream at large angles of incidence, where the largely separated wake induces unsteady pressure fluctuations. However, noise scaling with the deflection angle of wall-mounted flat plates remains lacking.
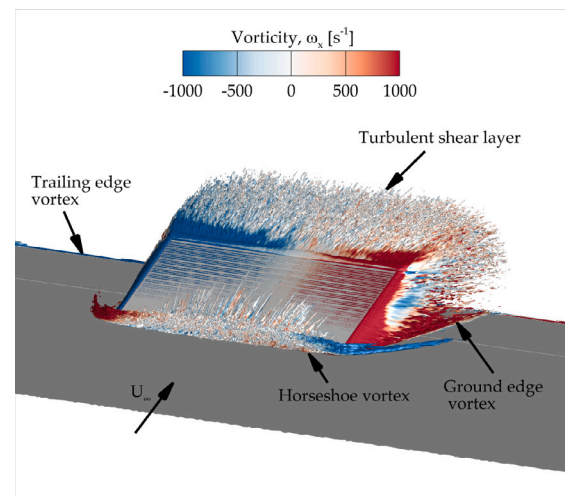

Fig. 1. Flow topology for a wall-mounted flat plate on a non-lifting surface at a deflection angle of $\delta_{fp} = 30°$, highlighting the main vortical structures generated by the inclined plate (Parnis and Angland, 2025).

The flow topology around wall-mounted bodies exhibits complex three-dimensional fluid phenomena. Acoustic research conducted for wall-mounted spoiler plates by Parnis and Angland (2025) showed that the acoustic sources for a wall-mounted flat plate can be characterized by the pressure fluctuations due to the upstream horseshoe vortex, the ground edge vortices and the turbulent wake. For a deflection angle of $\delta_{fp} = 30°$, the ground edge vortices and the flat plate side-edge were found to be the dominant acoustic noise source, in particular at high frequencies. The upstream horseshoe vortex is analogous to those seen in junction flows of wall-mounted prisms (Becker et al., 2002), formed due to upstream boundary layer separation due to the adverse pressure gradient induced by the inclined flat plate, whose strength is dependent on the deflection angle of the flat plate. This upstream separation vortex structure induces unsteady wall pressure fluctuations along the separated region, reaching a maximum intensity at flow reattachment lines (Agui and Andreopoulos, 1990). These substantial on-surface pressure fluctuations contribute to the formation of an additional broadband noise source upstream of the body along the base mounting plate (Becker et al., 2008; Moreau and Doolan, 2013; Porteous et al., 2014).

While aerodynamic scaling laws for freestream plates are well established (Fage and Johansen, 1927; Flachsbart, 1932; Holmes et al., 2005; Ortiz et al., 2015; Pieris et al., 2022), no equivalent scaling framework exists for wall-mounted inclined plates, where additional wall-induced effects influence the aerodynamic and noise characteristics of the inclined plate. This knowledge gap motivates the present study, which aims to establish scaling relationships for aerodynamic loads and farfield acoustics of a wall-mounted inclined flat plate with a fixed aspect ratio. This work examines how aerodynamic loads and aerodynamically generated noise varies with deflection angle, projected frontal area, and freestream velocity to provide both design guidance and insight into the flow–acoustic mechanisms of these commonly used industrial geometries.

The paper is structured as follows. Firstly, the experimental methodology is presented, describing the wall-mounted flat plate wind tunnel model used and the experimental acquisition methods. Since the experiments were performed in a Kevlar test section, a correction method is introduced and calibrated with experimental data to correct the aerodynamic forces for solid and wake blockage. The results section investigates the scaling relationship of the aerodynamic loads and farfield acoustics for the baseline wall-mounted inclined flat plate with an aspect ratio of 2.3 as a function of flat plate deflection angle, δ_{fp}.

The acoustic relationship is determined as a function of the integrated acoustic intensity, L_I, for variations in projected area and freestream velocity.

2. Experimental approach

The experiments were conducted at the anechoic wind tunnel facility at the University of Southampton (SotonAWT). The tunnel is an open jet, closed return wind tunnel with a nozzle cross-section of 0.75 m × 1 m. In an empty test section, the maximum freestream velocity of the tunnel is approximately 80 m/s. The anechoic chamber is fitted with acoustic wedges and is anechoic down to a frequency of 250 Hz. These wind tunnel experiments were conducted at a freestream velocity up to 70 m/s.

2.1. Kevlar-walled hybrid test section

The experiments were performed in a hybrid Kevlar test section shown in Fig. 2. The reason for choosing this configuration of wind tunnel over the open jet configuration was to minimize the effect of wake deflection on the background noise. The background noise is typically measured with an empty test section. The flat plate model deflected the open jet depending on the deflection angle of the plate. This jet then interacted differently with the collector of the wind tunnel, depending on the deflection angle, resulting in some uncertainties of the background noise levels, especially at low frequencies. In order to minimize these uncertainties, a Kevlar test section was used, which constrains the deflected wake and behaves more like a closed wall test section while still allowing acoustic waves to propagate through the Kevlar panels, albeit with some attenuation. However, the effect of the Kevlar test section is to introduce some solid and wake blockage effects on the aerodynamic forces. Force data was also collected in an 3/4th open test section configuration in order to be able to quantify the effect of wake confinement on the aerodynamic forces. The aerodynamic corrections, done to correct for the solid and wake blockage, are based on the bluff body corrections done in closed test section wind tunnels, firstly introduced by Maskell (1963) and later expanded on by Hackett (1996). These are extended, in this work, to account for the permeability of the Kevlar test section.

The hybrid Kevlar test section, shown in Fig. 2, extends the nozzle of the open-jet wind tunnel using tensioned acoustic-permeable Kevlar panels in place of solid walls. The test section's structure is made of an aluminium skeleton connected to the existing nozzle of the open jet wind tunnel. This maintains the internal dimensions of the nozzle. The length of the test section is 2.3 m allowing for a small gap between the test section and the collector. Custom-designed panels support plain-weave Kevlar cloth (0.12 mm thickness, 61 g/cm^2 specific weight) tensioned at 1500 N/m. Acoustic corrections were implemented to account for the influence of the Kevlar test section on the results. Acoustic corrections are based on work done by Devenport et al. (2013), and have been implemented to correct for acoustic transmission loss through the tensioned Kevlar material and through the thin boundary layer growing along the Kevlar panels.

2.2. Wall-mounted inclined flat plate model configuration

The finite span, wall-mounted flat plate rectangular model was constructed from a thin steel plate with a chord of $c = 106$ mm and a span $b = 247$ mm. The aspect ratio of the plate is equal to 2.3. The thickness of the plate is $t = 6$ mm. In addition, no edge rounding was performed on the flat plate's sharp edges.

To analyse the effects of deflection along the direction of the incoming flow stream, two brackets were connected to the base region of the downstream face of the flat plate at a spanwise location of $\pm 0.22b$ from the flat plate's centre line. The brackets were designed to minimize any aerodynamic interference occurring with the downstream flow field of

Fig. 2. Kevlar-walled hybrid test section.

the plate. To allow for aerodynamic load transfer from the plate to the load cell, the brackets were connected to a mounting block fixed on the inertial frame of the wind tunnel structure. The plate was deflected through a deflection angle, δ_{fp} between 10° and 90° at 10° intervals. The angles were positively located using pre-manufactured holes along a mounting block, providing good repeatability for the deflection angle of the flat plate. The flat plate model schematic is shown in Fig. 3, with the deflection angle, δ_{fp}, measured between the flat plate (deflected in the same direction as the freestream velocity vector) and the base mounting plate. The test was conducted at freestream velocities of 40 m/s to 70 m/s. These correspond to a Reynolds number between 2.9×10^5 and 5.1×10^5 based on the chord length of the plate.

The model was mounted on a base plate positioned in the upstream section of the Kevlar test section as shown in Fig. 4. The plate's leading edge was flush-mounted with the nozzle flange, with tensioned Kevlar panels installed along the remaining sides of the test section, allowing for acoustic measurements to be done along the overhead arc. The flat plate was located 702 mm downstream of the beginning of the Kevlar test section (dimension x_{LE} in Fig. 3).

A small gap was designed between the leading edge of the flat plate and the base plate. This was done to ensure that all the aerodynamic loads on the flat plate were fully transferred to the load cell. The gap size, g, between the leading edge and the base plate varied with the deflection angle of the flat plate model up to a maximum gap ratio of $g/c = 0.032$. The height of the gap was measured using a feeler gauge at three different locations along the span of the flat plate model and then averaged. The boundary layer thickness ratio at the position of the flat plate's leading edge is equal to δ/g of 14, and a boundary layer thickness to chord ratio, δ/c, equal to 0.26. The presence of the inclined flat plate introduces an adverse pressure gradient upstream of it as a function of the deflection angle. Such an adverse pressure thickens the boundary layer upstream of the flat plate. As a result, the gap is immersed significantly within the boundary layer, where the velocities are significantly lower than the freestream velocity. In the design of the experimental setup, numerical simulations were performed to aid the
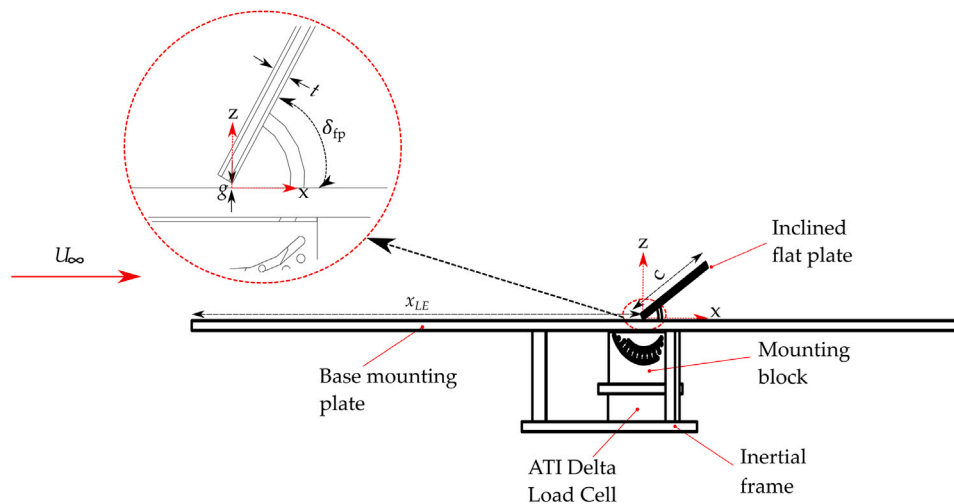
Fig. 3. Wall-mounted flat plate model schematic.

design of the setup. Simulations were performed both with and without the hinge gap present. These showed that the effect of this small gap on the aerodynamic loads was very small (less than the experimental uncertainty in the loads). The effect on the acoustic measurements will be discussed later.

2.3. Acquisition methodology

Force and acoustic measurements were conducted to analyse the scaling laws at different deflection angles and velocities. Aerodynamic loads and moments exerted on the model were measured using an ATI Delta 6-component transducer (ATI Industrial Automation, 2021) connected to the inertial frame of the wind tunnel. The direction of the lift and drag forces were along the positive z and x axes, respectively, according to the coordinate axis shown in Fig. 3. Measurements were taken at a sampling rate of 1 kHz. The dynamic pressure used in the calculation of the force coefficients was acquired using a Furness controls FCO332-4W differential transducer, having an uncertainty less than $\pm 0.5\%$ of the measured reading. The freestream dynamic pressure in the test section was determined using the pressure differential between two static ring measurements along the nozzle contraction. The differential pressure was calibrated with respect to the dynamic pressure measured at 0.5 m downstream of the nozzle (Ivanova and Angland, 2022). The experimental uncertainty of the aerodynamic loads was assessed by calculating the Type A and Type B uncertainties (JCGM, 2008). These uncertainties are shown in the key plots as a function of deflection angles and Re number.

Acoustic measurements of the flow-induced noise generated by the inclined flat plate for a given Re number and deflection angle were conducted using an overhead far-field microphone array. A total of ten GRAS 1/4" 46BE microphones were used. The constant current power, free-field microphones are capable of resolving a frequency range from 4 Hz to 80 kHz, with a dynamic range of 35 dB (A) to 160 dB and a sensitivity of 3.6 mV/Pa. The microphone setup is shown in Fig. 4.

Ten microphones were set up along the overhead arc of the model to capture a polar arc for angles between 67° and 113°, where $\theta = 90°$ corresponds to the location directly above the flat plate's leading edge. The vertical distance, z, between the model's coordinate system, highlighted in Fig. 2, and the overhead microphone was approximately $z = 1.33$ m. To account for the directivity of the flow-induced noise source, the scaling measurements presented were calculated as a function of the integrated acoustic intensity from all the microphones along the overhead arc. The physical locations of the microphones with respect to the model coordinate axis specified in Fig. 2 are provided in Appendix in Table A.1.

3. Aerodynamic loads and scaling for a wall-mounted inclined flat plate

This section analyses the aerodynamic loads and scaling behaviour of an inclined flat plate mounted on a flat surface. The investigation has two primary objectives. The first is to provide an understanding of how the loads of a wall-mounted flat plate vary as a function of deflection angle and the second is to establish a simple scaling law for predicting the drag and lift coefficients of an inclined wall-mounted flat plate that can be used for preliminary engineering design work.

The section is structured in three parts. The first addresses the aerodynamic corrections implemented to account for solid body and wake blockage generated by the inclined flat plate at varying deflection angles when tested in a hybrid kevlar test section. The blockage correction is presented for $Re = 4.3 \times 10^5$, corresponding to $U_\infty = 60$ m/s. The second examines the aerodynamic characteristics in terms of the normal force coefficient, C_N and the normalized normal force coefficient, C_N^*, where normalization is performed relative to the projected area for a given deflection angle. The final part introduces a simple scaling law to predict the aerodynamic coefficients of a wall-mounted flat plate where pressure forces dominate.

3.1. Aerodynamic test section blockage correction

When the model blockage ratio between the projected area of the model and the test section approaches values of $\approx 5\%$, the aerodynamic coefficients obtained from wind tunnel testing of wall-mounted bodies require correction to account for solid body and wake blockage effects. This section details the methodology to correct the aerodynamic measurements obtained in the Kevlar-walled hybrid test section. The correction approach combines established bluff body blockage theories with specific adaptations to account for the permeability of the Kevlar walls, calculated uniquely through optimizing agreement with measurements done in an open-test section configuration.

Test section blockage corrections for Kevlar hybrid test sections have primarily been developed for lifting bodies, as presented by Devenport et al. (2010, 2013). In these applications, solid-wall interference corrections derived from two-dimensional thin airfoil theory for closed test sections (Allen and Vincenti, 1944) have been applied to correct on-surface pressure distributions for lifting wings and determine the effective angle of attack corresponding to free-flight conditions. To account for the porosity of the Kevlar panels, a porosity factor, Ω, is introduced as a multiplier to the solid body correction constant, ε_{solid}, as shown in Eq. (1) (assuming rigid porous walls (i.e., negligible wall deflection) (Ewald, 1998)). Since the blockage constant for a solid
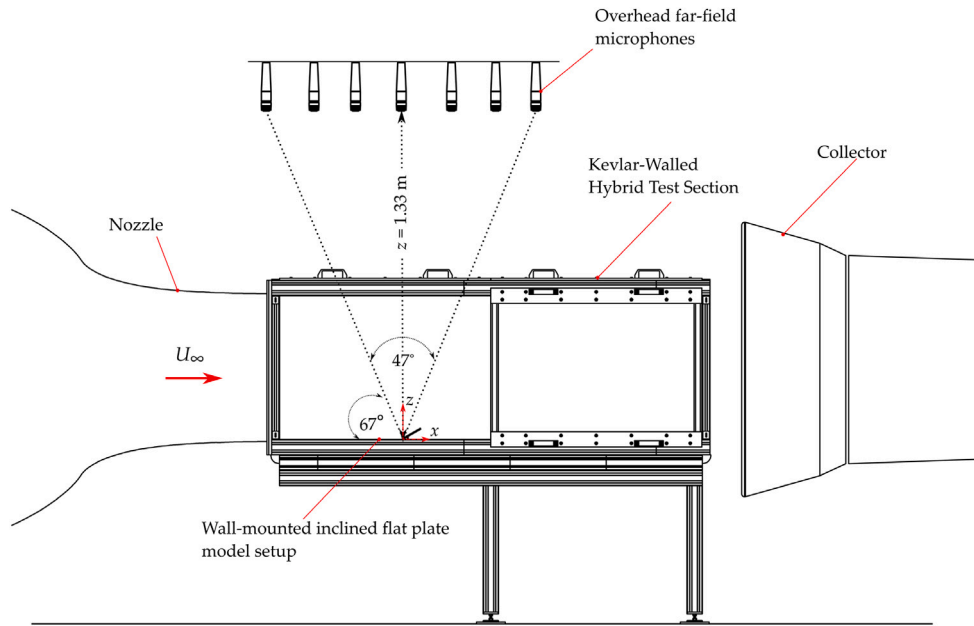
Fig. 4. Experimental setup schematic, including the Kevlar-walled hybrid test section, showing the physical location of the overhead far-field microphone array.

test section exceeds that for a porous section (assuming small wall deflections), the porosity ratio for a Kevlar test section $\Omega < 1$.

$$\varepsilon_{porous} = \Omega \, \varepsilon_{solid} \; . \tag{1}$$

Compared to a rigid closed test section, the hybrid test section with permeable Kevlar panels behaves as an intermediate open/closed configuration. The permeability of the panels allows some transpiration through the panels. The resulting pressure difference across the Kevlar panels may also cause the panels to deflect. These deflections can be substantial for certain model geometries, resulting in local variations of the test section cross-sectional area. Consequently, the porosity factor may diverge significantly from values typically associated with rigid closed wind tunnel walls (Devenport et al., 2010, 2013). As a result, no universal Ω exists for a given hybrid test section geometry, necessitating empirical determination of the correction factor for each model configuration and test condition.

For bluff body geometries, such as wall-mounted flat plates, the lifting-body correction methodology cannot be used. This is due to the assumption of predominantly attached flow on the wind tunnel model. A wall-mounted flat plate generates a large separated wake that expands as it convects downstream, constrained by the dimensions of the test section. This necessitates the application of both solid body and wake blockage corrections. For bluff bodies in solid closed test sections, corrections are based on the analysis presented by Maskell (1963) and later expanded by Hackett (1996) to include the impact of wake distortion.

The methodology presented by Maskell (1963), presents a dynamic pressure correction formulation as shown in Eq. (2).

$$\frac{q_c}{q_u} = \frac{C_{D_u}}{C_{D_{M_1}}} = 1 + \varepsilon_{solid} C_{D_u} (S/C) \; . \tag{2}$$

In Eq. (2), C_{D_u}, represents the measured pressure drag, q_u the measured dynamic pressure, q_c the corrected dynamic pressure, and $C_{D_{M_1}}$ is the corrected drag coefficient based on the single-stage Maskell Equation. The correction incorporates the model blockage ratio in terms of the model's projected area, S and the test section cross-section area, C. For flat plates, the bluff body blockage constant, ε_{solid} for a solid closed test section can be estimated using Eq. (3), where AR represents the projected aspect ratio of the plate at a given deflection angle (defined in Eq. (4)). Since the profile drag of wall-mounted plates

is dominated by pressure drag, C_{D_u} is considered equivalent to the drag coefficient measured directly in the hybrid test section.

$$\varepsilon_{solid} = 0.96 + 1.94 \exp(-0.06\text{AR}) \; . \tag{3}$$

$$AR = \frac{b}{c \sin \delta_{fp}} \; . \tag{4}$$

Hackett (1996) expanded Maskell's analysis by decomposing the correction into two components: blockage-induced incremental velocity (correction of the incoming dynamic pressure) and a drag increment due to wake distortion due to wake constraint effects (based on assumptions established in Maskell, 1963). This decomposition enables more accurate drag correction (Ewald, 1998). The resulting two-step version of Maskell's analysis yielding $C_{D_{M2}}$ is presented in Eq. (5).

$$C_{D_{M2}} = \frac{C_{D_u} + \Delta C_{DM}}{q_c / q_u} = \frac{C_{D_u} + \Delta C_{DM}}{1 + \varepsilon_{solid}(C_{D_{M1}} - \Delta C_{DM})(S/C)} \; . \tag{5}$$

In Eq. (5), $C_{D_{M2}}$ represents the corrected drag coefficient derived from the extended two-step Maskell analysis, and ΔC_{DM} denotes the drag increment attributable to wake distortion. A closed form of the equation of the drag increment, ΔC_{DM} is presented in Eq. (6).

$$\Delta C_{DM} = \frac{C_{D_u}}{(1 + \varepsilon_{solid} C_{D_u}(S/C))} + \left[\frac{C_{D_u}}{2\varepsilon_{solid} C_{D_u}(S/C)} \right] \left[1 - \sqrt{1 + 4\varepsilon_{solid} C_{D_u}(S/C)} \right] \; . \tag{6}$$

The lift coefficient correction C_{L_c} (expressed in Eq. (7)) is applied solely based on the dynamic pressure correction of the incoming flow field, as determined by Eq. (2). It is important to note that this formulation to determine the C_{L_c} only addresses solid and wake blockage through dynamic pressure correction, but does not account for lift interference and streamline curvature errors induced by flow containment by the hybrid test section walls (Joppa, 1973).

$$C_{L_c} = \frac{C_{L_u}}{q_c / q_u} \; . \tag{7}$$

Fig. 5 presents a comparison of the uncorrected and corrected drag coefficients calculated using the correction method described by Eq. (5), as a function of deflection angle, δ_{fp}, at $Re = 4.3 \times 10^5$. Since blockage correction varies with the projected aspect ratio (defined in Eq. (4)), the correction magnitude is small for deflection angles below $\delta_{fp} = 40°$, becoming progressively greater at larger angles where the
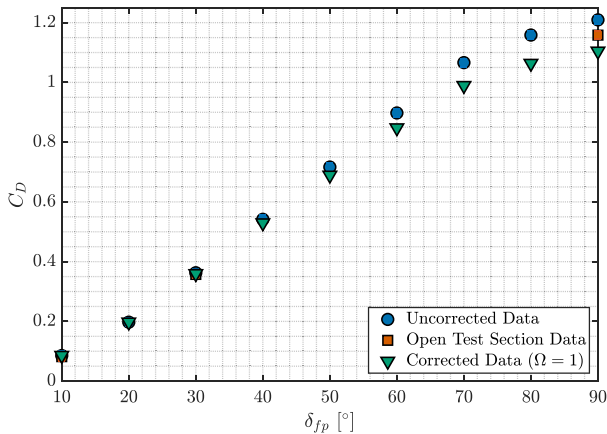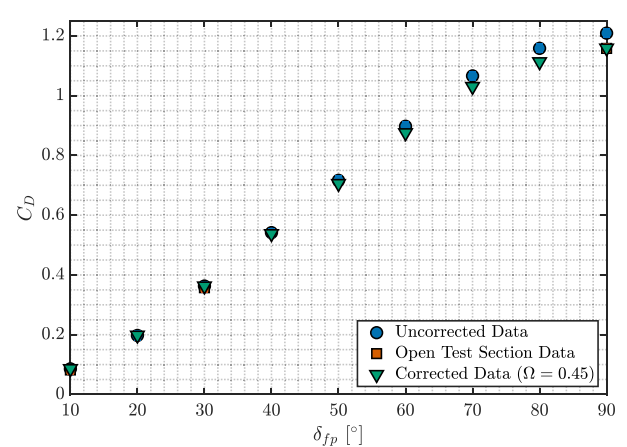
Fig. 5. Comparison of drag coefficient, C_D, as a function of deflection angle, δ_{fp}, at $Re = 4.3 \times 10^5$. ● uncorrected data measured in the hybrid test section, ■ data measured in an open test section, ▼ corrected results using Eq. (5) (Hackett, 1996) with a porosity factor $\Omega = 1$.

blockage ratio between model and test section area increases. This results in a maximum correction of $\Delta C_D = -0.12$ at a deflection angle of $\delta_{fp} = 90°$.

To assess the validity of the blockage correction calculated, Fig. 5 compares the corrected C_D results calculated in the Kevlar hybrid test section with those obtained for a similar configuration tested in an open test section configuration, where the model was flush mounted to the nozzle of the open jet wind tunnel, forming a 3/4th open test section. Ewald (1998) highlighted that the measurements in open test sections typically exhibit minimal blockage effects compared to closed test sections, and hence open test section results can be used as a representative data set to assess the influence of the permeability of the test section.

The open test section dataset comprises a subset of drag coefficient, C_D measurements at three distinct deflection angles of $\delta_{fp} = 10°$, $30°$ and $90°$. Comparison between these measurements and the corrected hybrid test section data reveals that the implemented blockage correction over-corrects at high deflection angles, while showing good agreement at low deflection angles where blockage effects are minimal. The over-correction at large deflection angles can be attributed to using a porosity factor of $\Omega = 1$, suggesting that the walls of the test section are completely solid. This is not the case for the permeable Kevlar panels.

In this work, the porosity factor, Ω, is calculated using a similar methodology that (Devenport et al., 2010) used for lifting bodies, but with two unique differences due to the bluff body investigated in this work. The first is that the correction is based on the bluff body blockage corrections of Maskell (1963). The second is that open test section experimental data is used to determine the porosity factor, Ω, instead of numerical simulations for a lifting wing in free-field conditions. The porosity factor, Ω, corrects for the difference between the drag measured in a hybrid test section and that obtained, for a similar configuration, measured in an open test section. While theoretically the value of the porosity factor constant will be different for every deflection angle, consistent with Devenport et al. (2013), a single value is used for this study. Hence, the calibration of this constant was done for a deflection angle of $\delta_{fp} = 90°$, which showed the largest deviation from the open test section results. Due to the decrease in projected frontal area as the deflection angle reduces, the blockage correction becomes less significant at lower deflection angles. Considering Eq. (2), the value of Ω can be calculated by equating the corrected drag coefficient, $C_{D_{M1}}$
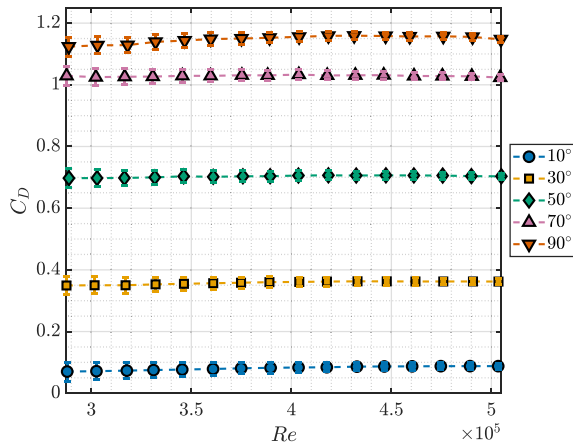

(a) Drag Coefficient, C_D
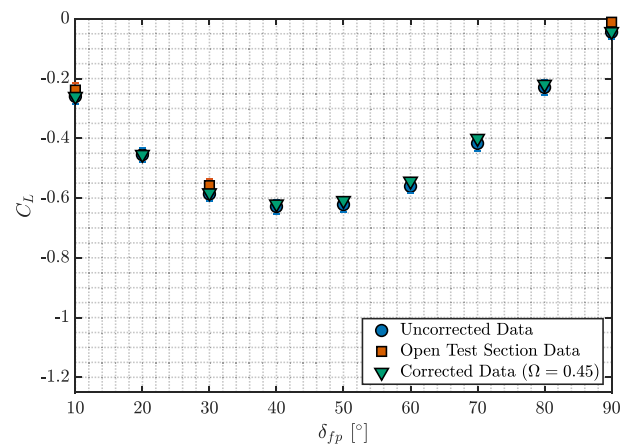
(b) Lift Coefficient, C_L

Fig. 6. Comparison of the drag coefficient and lift coefficient as a function of deflection angle, δ_{fp}, at $Re = 4.3 \times 10^5$. ● uncorrected data as measured in the hybrid test section, ■ data measured in an open test section, ▼ corrected results using a porosity factor $\Omega = 0.45$.

to the measured drag coefficient at $\delta_{fp} = 90°$ in an open test section, $C_{D_{open}}$. The final equation is expressed in Eq. (8).

$$\frac{C_{D_u}}{C_{D_{open}}} = 1 + \Omega \varepsilon_{solid} C_{D_u}(S/C) \ . \tag{8}$$

In Eq. (8), C_{D_u} is the uncorrected drag coefficient measured in the hybrid test section, ε_{solid} is the solid body correction, S is the model's projected area, and C is the test section cross-section area. This result yields a porosity factor of $\Omega = 0.45$, which aligns with values reported in literature for lifting wings where wall deflections were limited (Devenport et al., 2010). Fig. 6(a) demonstrates that drag forces corrected using this porosity factor show excellent agreement with the open test section dataset, at all three different deflection angles where open test section data was available. The agreement in the lift force is not as good between the open test section results and the corrected hybrid test section results as shown in Fig. 6(b). The corrected data is closer to the open test section data than the uncorrected data, but still under-predicts it slightly. The current methodology only addresses solid and wake blockage through a dynamic pressure correction, but does not account for lift interference and streamline curvature errors

(a) Drag Coefficient, C_D
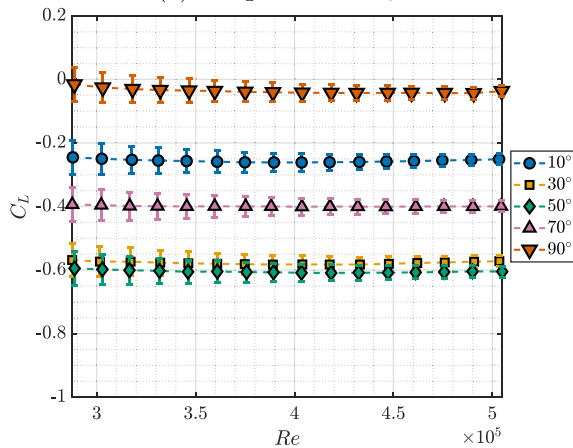
(b) Lift Coefficient, C_L

Fig. 7. Variation of the aerodynamic load coefficients with Re number based on chord length, as a function of flat plate deflection angle, δ_{fp}.

induced by flow containment (Joppa, 1973). This is a limitation of the proposed method.

3.2. Reynolds number scaling for inclined flat plates

The influence of the Reynolds Number, Re, on the aerodynamic performance of the inclined plate across various deflection angles is shown for the corrected drag coefficient, C_D and lift coefficient, C_L results in Figs. 7(a) and 7(b), respectively. A representative subset of the deflection angle range studied is presented. All of the deflection angles follow a similar trend.

Hoerner (1965) found that the drag coefficient for flat plates in freestream was independent of Reynolds number. This behaviour was attributed to the fixed separation points along the edges of the inclined plate. The independence with Reynolds number is seen in the force data for a wall-mounted flat plate in Fig. 7(a) and Fig. 7(b) for most deflection angles. There are slight deviations in both lift and drag at the lowest Reynolds numbers for some specific deflection angles, e.g. at a deflection angle of 90°. However, these deviations are within the uncertainty in the force measurements, which increase at lower Reynolds numbers. Therefore, within the experimental uncertainty of the force data, both the lift and drag are approximately independent of Reynolds number for this wall-mounted case, similar to what is seen for flat plates in freestream.
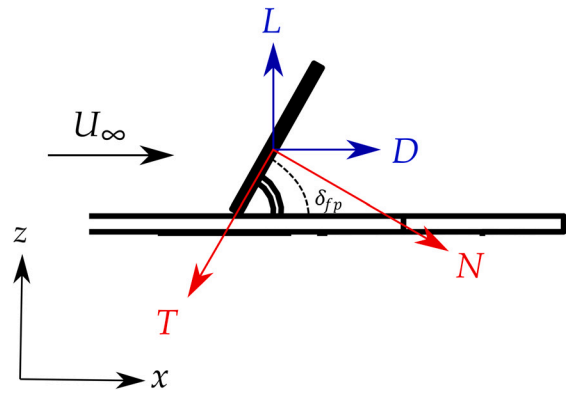

Fig. 8. Generalized schematic of the force decomposition of the lift, L and drag, D forces and the normal, N and tangential, T forces acting on an inclined wall-mounted flat plate.

3.3. Aerodynamic load scaling analysis

One of the objectives of this work is to define aerodynamic scaling laws for a wall-mounted flat plate inclined in the direction of the freestream flow as a function of the deflection angle, δ_{fp}. Fig. 8 illustrates a schematic of the force decomposition acting on the inclined plate configuration, where the lift force, L, acts perpendicular to the freestream velocity and the drag force, D, acts parallel to it. In reality, due to the pressure difference, the flat plate produces downforce. Fig. 8 presents a generalized force decomposition applicable to various flat plate geometries at different ground clearances. To quantify the impact of deflection angle on aerodynamic loads, the scaling analysis is conducted in terms of normal force, N, which is calculated as a function of the drag and lift force components acting on the inclined flat plate and directly measured by the load cell.

The equations relating normal and tangential forces to the lift and drag forces produced by the inclined flat plate are given in Eqs. (9) and (10). As discussed later, the tangential force, T, generated by the plate was found to be negligible compared to the normal forces for the wall-mounted configuration.

$$N = D\sin(\delta_{fp}) - L\cos(\delta_{fp}) \ , \tag{9}$$

$$T = -D\cos(\delta_{fp}) - L\sin(\delta_{fp}) \ . \tag{10}$$

The aerodynamic normal force coefficient C_N, as a function of the deflection angle is shown in Fig. 9(a). Results were calculated for a reference planform area, A_{ref}, which was a constant for each deflection angle. The reference area, equal to the product of chord and span of the model ($c \times b = 0.026$ m^2) was used to calculate C_N according to Eq. (11).

$$C_N = \frac{N}{(q_\infty \times A_{\text{ref}})} \ . \tag{11}$$

The results (Fig. 9(a)) show an increase of the normal force coefficient with increasing deflection angle approaching a value which is a maximum at $C_N = 90°$. These findings are compared with published data for 2D inclined flat plates in freestream (Fage and Johansen, 1927) and 3D inclined flat plates, with similar aspect ratios, in freestream (Ortiz et al., 2015; Pieris et al., 2022). Although the aspect ratios of the 3D flat plates differ slightly, Fail et al. (1959) demonstrated that for normal low-aspect-ratio plates in freestream, changes in aerodynamic performance (drag, base pressure and recirculation bubble length) are small for aspect ratios up to 10. The data for the wall-mounted case collapses with the freestream plate values in literature (for similar aspect ratios $AR \approx 2$) at deflection angles $\delta_{fp} > 30°$. For lower

deflection angles, where the C_L becomes dominant in the C_N equation (Eq. (9)), the experimental data for the wall-mounted plate shows lower C_N values than those reported in literature for plates in freestream. This discrepancy arises from the fundamentally different lift generation mechanisms for both the wall-mounted cases and the freestream cases at low deflection angles ($\delta_{fp} \leq 30°$). Another important distinction between the wall-mounted and freestream configurations is the presence of the base mounting plate that constrains the growth of the wake compared to the freestream case. In spite of these differences, at a deflection angle of 90°, the differences in normalized normal force coefficient, $C_N{}^*$, are relatively small.

For an inclined plate in freestream, the flat plate behaves similar to a thin airfoil, with lift generated by the pressure difference between the suction side (downstream face) and the pressure side (upstream face). At low to moderate angles of attack, the flow separating at the leading edge of the plate typically reattaches on the suction surface, producing negative lift or downforce (Pieris et al., 2022). In contrast, for a wall-mounted inclined plate, the leading edge is immersed in the upstream boundary layer, resulting in substantially reduced flow velocity through the gap between the mounting surface and the leading edge compared to freestream velocity. As a result the downstream face of the inclined flat plate is exposed to the base pressure of the massively separated flow downstream of the plate. Consequently, this leads to smaller lift magnitudes for the wall-mounted configurations. While, the normal force coefficient for a wall-mounted plate was similar to the values for plates in freestream at high deflection angles (for plates with similar aspect ratios), the main differences occurred at low deflection angles due to the changes in the lift force discussed above.

When comparing the wall-mounted experimental data with that for a 2D inclined plate ($AR = \infty$) in freestream from literature, a similar trend is observed at low deflection angle as shown in Fig. 9(a) where larger values of normal force are generated at low deflection angles. The difference in the plateau value of the C_N at high deflection angles between the 2D plate in freestream and the wall-mounted 3D plate is due to the increase in the C_D with increasing AR (Fail et al., 1956).

To assess the scaling behaviour of aerodynamic loads for the wall-mounted plate, a normalized normal force coefficient, $C_N{}^*$ was calculated with respect to the projected frontal area, A_{proj} for each deflection angle (defined in Eq. (13)). This normalization approach was implemented to evaluate how the projected area influences aerodynamic loads on the flat plate model. The normalized coefficient, $C_N{}^*$ is calculated using Eq. (12).

$$C_N{}^* = \frac{N}{(q_\infty \times A_{\mathrm{proj}})} \ , \tag{12}$$

where,

$$A_{\mathrm{proj}} = c \times b \times \sin(\delta_{fp}) \ . \tag{13}$$

Fig. 9(b) demonstrates the collapse of the normalized normal force coefficient data when scaled with the projected frontal area. For deflection angles above the stall angle, where the downforce begins to decrease ($\delta_{fp} \geq 40°$), the experimental data converges to an approximately constant $C_N{}^*$ value equal to that observed at a deflection angle of $\delta_{fp} = 90°$. This convergence is represented by the dashed trend-line in Fig. 9(b) for each dataset. This value corresponds to the maximum drag coefficient obtained when the plate is normal to the flow at a deflection angle of 90°. A similar collapse is observed for the freestream plate data in literature with similar aspect ratios at high deflection angles.

For deflection angles below 30°, the data diverges from the maximum $C_N{}^*$ value (shown by the dashed line in Fig. 9(b)). Since the downforce generated by wall-mounted flat plates at low deflection angles is substantially smaller than that generated in freestream conditions, the difference between the $C_N{}^*$ values at low deflection angles and the maximum value at $\delta_{fp} = 90°$ remains below $C_N{}^* < 0.4$. This
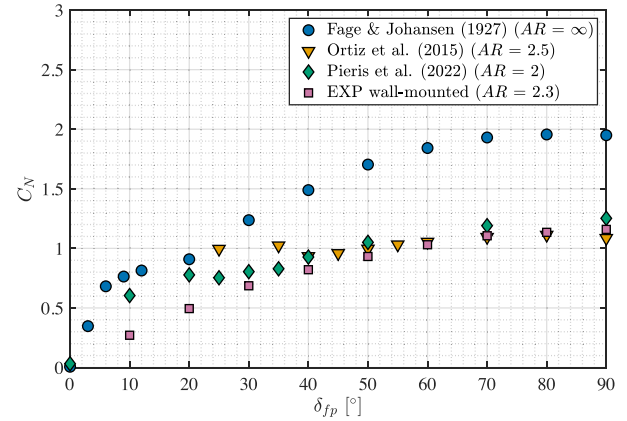
(a) Normal force coefficient, C_N.
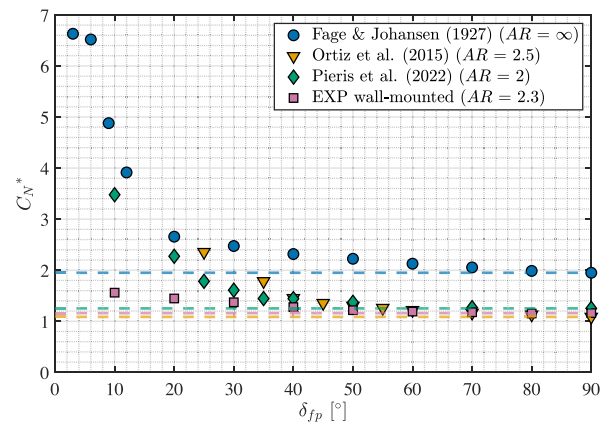
(b) Normalized normal force coefficient, $C_N{}^*$, based on the projected frontal area. Dotted line represents the maximum value of $C_N{}^*$, i.e. $C_N{}^*$ at 90°.

Fig. 9. Normal force coefficient, C_N, and the normalized normal force coefficient, $C_N{}^*$, for a wall-mounted inclined flat plate as a function of deflection angle at $Re = 4.3 \times 10^5$. Results are compared with data from literature for inclined flat plates in freestream for a 2D case (Fage and Johansen, 1927) and similar aspect ratios in freestream $AR \approx 2$ (Ortiz et al., 2015; Pieris et al., 2022).

behaviour is different to that observed for flat plates in freestream. Since the normalized normal force coefficient $C_N{}^*$, varies so little for the wall-mounted case, it is possible to propose a scaling model for the lift and drag forces on wall-mounted flat plate configurations. The same scaling model cannot be used for plates in freestream due to the differences in $C_N{}^*$ at low deflection angles, resulting from the larger lift forces generated by plates in freestream, as discussed previously.

To develop a prediction method for wall-mounted flat plates, and assuming negligible viscous forces compared to pressure forces (and thus negligible C_T), the aerodynamic loads of a flat plate inclined at a given deflection angle can be predicted using the following procedure. First by substituting the value of the C_D at $\delta_{fp} = 90°$ in Eq. (14) the value of the predicted normal force coefficient, $C_{N_{\mathrm{pred}}}$ is determined.

$$C_{N_{\mathrm{pred}}} = C_N{}^* \sin(\delta_{\mathrm{fp}}) = C_{D_{\mathrm{meas}(90°)}} \sin(\delta_{\mathrm{fp}}) \ , \tag{14}$$

Subsequently, as the tangential force, C_T, is assumed to be negligible, the dimensionless tangential force equation (Eq. (10)) can be

written as,

$$C_T = 0 = -C_{D_{\text{pred}}} \cos(\delta_{\text{fp}}) - C_{L_{\text{pred}}} \sin(\delta_{\text{fp}}) , \tag{15}$$

Solving for the predicted lift coefficient gives,

$$C_{L_{\text{pred}}} = -\frac{C_{D_{\text{pred}}}}{\tan(\delta_{\text{fp}})} . \tag{16}$$

Substituting the predicted lift coefficient (Eq. (16)) into the dimensionless form of the normal force equation (Eq. (9)) gives the following relationship for the predicted normal force coefficient,

$$C_{N_{\text{pred}}} = C_{D_{\text{pred}}} \sin(\delta_{\text{fp}}) - \left(-\frac{C_{D_{\text{pred}}}}{(\tan \delta_{\text{fp}})} \right) \cos(\delta_{\text{fp}}) . \tag{17}$$

Noting that $C_{N_{\text{pred}}}$ is simply calculated using Eq. (14) and the drag force at a deflection angle of 90°, the predicted drag can be solved as follows,

$$C_{D_{\text{pred}}} = \frac{C_{N_{\text{pred}}}}{\sin(\delta_{\text{fp}}) + \frac{\cos(\delta_{\text{fp}})}{\tan(\delta_{\text{fp}})}} = C_{N_{\text{pred}}} \sin(\delta_{\text{fp}}) . \tag{18}$$

Substituting the result of Eq. (18) in Eq. (16), $C_{L_{\text{pred}}}$ can be simplified as shown in Eq. (19).

$$C_{L_{\text{pred}}} = -\frac{C_{N_{\text{pred}}} \sin(\delta_{\text{fp}})}{\tan(\delta_{\text{fp}})} = -C_{N_{\text{pred}}} \cos(\delta_{\text{fp}}) . \tag{19}$$

The procedure is to calculate the predicted normal force using Eq. (14) and the drag force at a deflection angle of 90°. The predicted drag, $C_{D_{\text{pred}}}$, is estimated using Eq. (18). Finally the predicted lift, $C_{L_{\text{pred}}}$ is estimated using Eq. (19).

The results of the force scaling laws are shown in Fig. 10. The scaling relationship demonstrates good agreement between the measured and the predicted values, with maximum absolute errors of $\Delta C_D \leq 0.073$ and $\Delta C_L \leq 0.081$ across the calculated angle range. It is important to note that the scaling law is only for wall-mounted flat plates. It can also be used for plates in freestream for high deflection angles beyond stall ($\delta_{fp} > 40°$), where the normalized normal force coefficient, C_N^* collapses with the drag coefficient, C_D at a deflection angle of 90°. However, for low deflection angles ($\delta_{fp} \leq 40°$), plates in freestream generate higher lift, leading to the measured C_N^* values to be significantly larger than those calculated using the method proposed above.

This scaling law provides designers with a practical method to estimate the aerodynamic performance of wall-mounted inclined plates with aspect ratios $AR > 1.5$, by requiring only the drag coefficient of the plate at $\delta_{fp} = 90°$. Such an approach is particularly valuable during preliminary design stages when rapid assessment of various configurations is needed without requiring extensive computational or experimental resources.

4. Far-field acoustic scaling for wall-mounted flat plates

The previous section detailed how the aerodynamic forces on a wall-mounted flat plate varied with Reynolds number and deflection angle. A scaling law was proposed for how the aerodynamic forces varied as a function of deflection angle. For some engineering applications, the noise generated by wall-mounted flat plates is also an important design consideration. The goal of this section is to provide acoustic scaling laws. A similar structure to the previous section is followed here. Firstly, the acoustics generated by the inclined wall-mounted flat plate are analysed for various deflection angles and Reynolds numbers. For the aerodynamic loads analysis, a scaling relationship existed that can approximate the aerodynamic loads for a flat plate at a given deflection angle with the projected frontal area of the flat plate. The second part of this section is to determine similar scaling laws for the far-field acoustics for wall-mounted flat plates. There are two different scaling laws for the acoustics. The first relationship is with respect to the freestream velocity, U_∞, and the second is as a function of the
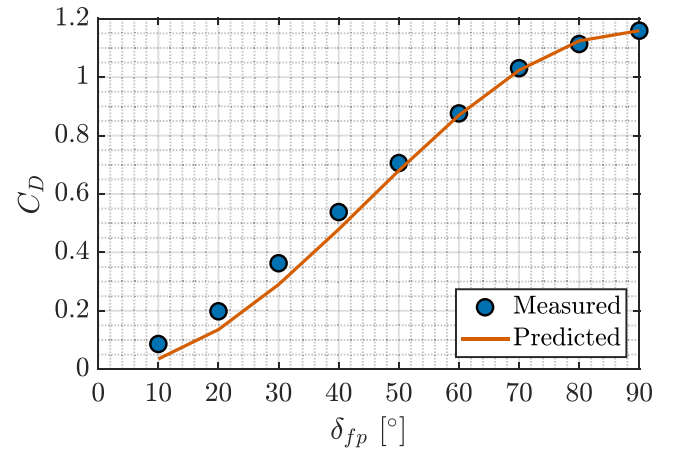
(a) Drag Coefficient, C_D.
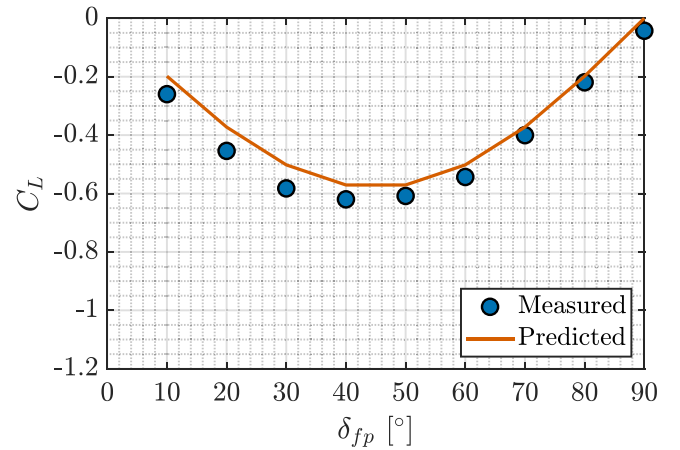
(b) Lift Coefficient, C_L.

Fig. 10. Comparison between the measured and the predicted aerodynamic coefficients as a function of deflection angle at a $Re = 4.3 \times 10^5$.

projected frontal area of the plate. Consequently, the conclusions from the two scaling relationships can be used to provide initial estimates of the noise generated by the wall-mounted inclined flat plates, but also to give an insight into the noise sources responsible for the far-field noise.

The spectrum of a wall-mounted flat plate is broadband in nature and does not contain discrete narrowband tones (Parnis and Angland, 2025). Due to the shear layer of opposite sign vorticity being inhibited from forming due to the mounting plate, there is no coherent bluff body vortex shedding in the wake. This is also consistent with the findings for plates adjacent to bounding surfaces placed normal to the flow (Everitt, 1982). Therefore, only one-third octave band data is presented here. The acoustic data was processed using a Hamming windowing function with 75% overlap at a sampling frequency of 25.6 kHz and an FFT block size of 4096.

The noise generated by the flat plate has a directivity. Plates in freestream typically have a dipole directivity pattern (Maruta and Kanagawa, 1981). The normal force on the flat plate varies with deflection angle and therefore the dipole axis also rotates as a function of deflection angle. This consequently alters the direction of maximum sound radiation. These changes in directivity mean that measurements taken at a fixed microphone location may give inconsistent scaling laws due to the changes in directivity for different deflection angles.

To account for the changes in directivity of the noise source at different deflection angles, the scaling was done in terms of the integrated sound intensity level, $L_{I_{\text{int}}}$, obtained by integrating the acoustic
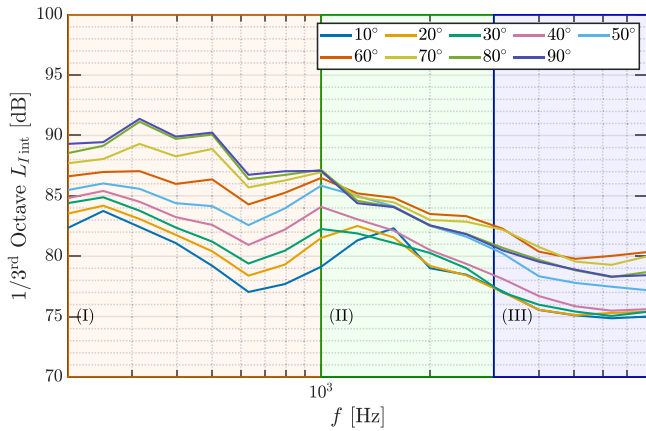
Fig. 11. Integrated acoustic intensity (defined in Eq. (20)) as a function of deflection angle, δ_{fp}, at $Re = 4.3 \times 10^5$.
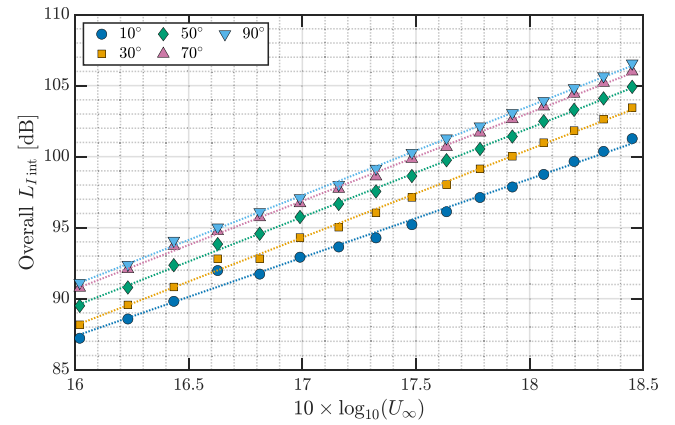

Fig. 12. Freestream velocity scaling plot for the overall integrated acoustic intensity for different deflection angles ($10° \leq \delta_{fp} \leq 90°$).

intensity from $67° \leq \theta \leq 113°$ in the arc shown in Fig. 4. Due to the limited number of microphones, the true source power level cannot be determined, and hence some directivity characteristics of the noise source may still not be fully captured. However, the integrated acoustic intensity is more robust than simply taking fixed microphone positions, as some directivity effects are included.

The quantity presented in the analysis is the integral of the acoustic intensity over the range of polar angles measured, assuming a homogeneous medium and that the wave fronts lie normal to the microphone arc plane.

$$L_{I \text{ int}} = 10 \log_{10}\left(\sum_{i=1}^{i=10} \left(p_i^2 / (\rho\, a) \right) \frac{\Delta S_i}{1 \times 10^{-12}} \right) . \tag{20}$$

In Eq. (20), ρ is the density, a is the speed of sound, p_i is the acoustic pressure measured at each microphone, i is the microphone index, and ΔS_i is the surface area of the microphone arc shown in Fig. 4.

One-third octave spectra of the integrated acoustic intensity for different flat plate deflection angles are presented in Fig. 11. These measurements are obtained at $Re = 4.3 \times 10^5$ (corresponding to $U_\infty = 60$ m/s). The flow around a wall-mounted flat plate is characterized by an arch-type broadband wake without any coherent vortex shedding. There is a horseshoe vortex that originates upstream of the flat plate and wraps around both sides of the flat plate. Inboard of the horseshoe vortex, there is a pair of ground vortices with the opposite sign vorticity to the horseshoe vortex (Parnis and Angland, 2025). This flow topology is shown in Fig. 1. The noise sources have previously been identified to be the broadband bluff body wake, the horseshoe vortex, as well as the ground edge vortices and the flat plate side-edges (Parnis and Angland, 2025). The upstream separation bubble and consequent horseshoe vortex formation will vary with deflection angle.

The spectra can be divided into three distinct frequency regimes, as highlighted in Fig. 11. Regime I encompasses frequencies below 1 kHz. In general, an increase in noise generated by the flat plate is observed with increasing deflection angle, with up to 11 dB difference between the lowest and highest deflection angles in the low frequency regime (below 1 kHz). However, the change in noise with deflection angles varies as a function of frequency. Numerical simulations done by Parnis and Angland (2025) for a wall-mounted flat plate at $\delta_{fp} = 30°$ revealed that low-frequency noise is dominated by the pressure fluctuations on the base mounting plate as a result of the flow field generated by the deflected flat plate. The noise contribution from pressure fluctuations on the flat plate surface itself was found to peak at approximately 1.25 kHz. This corresponds to Regime II, spanning 1 kHz$\leq f \leq 3$ kHz. Regime III contains the higher frequencies above 3 kHz.

As previously discussed, there was a small hinge gap between the mounting base plate and the inclined flat plate in order to measure the aerodynamic forces (Fig. 3). Supplementary experiments were performed to see the effect of this gap on the acoustic measurements by blocking this gap with tape (data omitted here for brevity). At deflection angles $\delta_{fp} > 20°$, there was an excellent agreement between the spectra, over the whole frequency range measured, suggesting this small gap immersed in the boundary layer was not a significant source of noise. At the smallest deflection angles ($\delta_{fp} < 20°$), there was some additional noise generated from 1 kHz to 5 kHz by the flow through the small gap. Outside of this particular frequency range, the agreement was very good for the acoustic spectra with and without the gap. This additional gap noise can be seen in the integrated acoustic intensity data in Fig. 11 for $\delta_{fp} = 10°$, centred around a one-third octave band of 1.25 kHz.

4.1. Acoustic scaling as a function of velocity

An analysis of the acoustic scaling with respect to freestream velocity was conducted to assess the noise source mechanisms of an inclined wall-mounted flat plate. The integrated acoustic intensity was plotted as a function of $10 \log_{10}(U_\infty)$ to determine how the integrated acoustic intensity scales with freestream velocity as a function of deflection angle. For a simple compact dipole source, the acoustic intensity should scale as U_∞^6 (Howe, 2003). This analysis was integrated across the entire frequency range. The experiments were conducted in the Kevlar-walled hybrid test section specifically to reduce the additional background facility noise that changed with deflection angle when the deflected flat plate's wake interacted with the wind tunnel collector, as explained previously. Results for deflection angles ranging from 10° to 90° in 20° increments are presented in Fig. 12. Not all deflection angles are included to improve the clarity of the figure. The trend is similar at the other deflection angles.

Linear regression analysis was performed for each deflection angle to quantify the acoustic velocity scaling. Table 1 summarizes the velocity scaling exponent, n_{U_∞}, as a function of deflection angle. As discussed above, the theoretical value for the velocity scaling exponent is 6 for a pure compact dipole. The slope of these regression lines for the wall-mounted flat plate varies approximately but not perfectly with U_∞^6. The imperfect collapse suggests that the noise generation mechanism for a wall-mounted flat plate is more complex than a simple dipole source, as the velocity exponent varies as a function of deflection angle.

At low deflection angles ($\delta_{fp} \leq 20°$), the velocity exponent is less than 6. The theoretical value for the velocity exponent for a pure edge scattering source is 5. Therefore, the noise source mechanism is a mixture of pure dipole and edge scattering.

Table 1
Variation of the velocity scaling exponent, n_{U_∞}, as a function of deflection angle, δ_{fp} from 10° to 90°.

δ_{fp} [°]	n_{U_∞}
10	5.5
20	5.9
30	6.2
40	6.3
50	6.3
60	6.2
70	6.2
80	6.2
90	6.3

This behaviour changes as the deflection angle increases and a stronger separation bubble forms upstream of the flat plate. For higher deflection angles ($\delta_{fp} > 30°$), the velocity exponent is slightly higher than the expected value for a pure compact dipole source. This is attributed to the turbulence modification along the upstream surface of the flat plate due to the additional impingement of the upstream separation bubble on the upstream face of the inclined flat plate. Similar behaviour was observed by Sundeep et al. (2022) for square obstructions in a turbulent boundary layer where the height of the obstacle was larger than the incoming boundary layer. Due to the complexity of the flow topology and resultant acoustic sources for wall-mounted flat plates, i.e. horseshoe vortex and ground edge vortices (shown in Fig. 1), the scaling with velocity is not a simple compact dipole source.

4.2. Acoustic scaling with respect to the projected area

To analyse the influence of the deflection angle on the flow-induced noise from wall-mounted flat plates, the integrated acoustic intensity was plotted as a function of $10\log_{10}(A_{proj}/A_{ref})$, where A_{proj} is the projected frontal area and A_{ref} is the planform area. Since this ratio is proportional to $\sin(\delta_{fp})$, the analysis provides an insight into how the integrated acoustic intensity scales with deflection angle. For a simple compact dipole source, the acoustic intensity should scale as a function of area to the power of unity (Howe, 2003). In this case, the projected frontal area is used as this is the quantity that varies with deflection angle. Similar to the velocity scaling analysis presented above, the scaling with projected area is expected to differ slightly from the theoretical value for a simple compact dipole due to the additional acoustic sources, non-compactness effects, edge scattering etc. The scaling analysis presented here will quantify this.

The integrated intensity spectra shown in Fig. 11 demonstrate that the scaling relationship for wall-mounted flat plates is not trivial and depends on both the frequency regime and the deflection angle of the flat plate. The velocity scaling in Section 4.1 identified that the noise source, while exhibiting scaling close to a dipole, is in reality a mixture of sources and the velocity scaling was dependent on the deflection angle.

Performing area scaling across the overall frequency range (shown in Fig. 13(a)) reveals two distinct scaling laws. One is for low deflection angles ($10° \leq \delta_{fp} \leq 30°$) and other is for higher deflection angles ($40° \leq \delta_{fp} \leq 90°$). Linear regressions were performed separately within each deflection angle range to determine the scaling exponent as a function of projected area. The corresponding slope variations across Re numbers are summarized in Table 2.

For the overall frequency range, the regression slope, n_A, demonstrates a clear difference between high and low deflection angles. At higher deflection angles ($\delta_{fp} \geq 40°$), n_A is approximately equal to 1.2. This is close to the theoretical value of unity expected for a simple compact dipole source. However, just like the velocity scaling
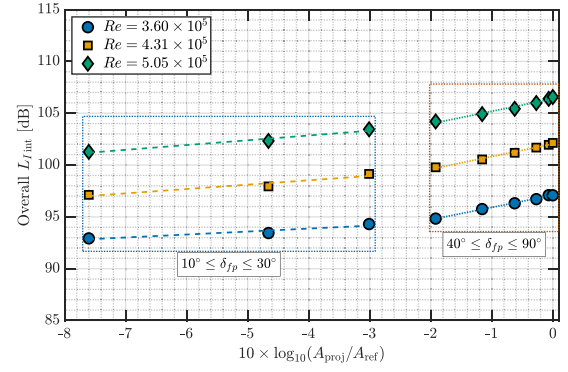
(a) Projected area scaling for overall integrated acoustic intensity as a function of different Re numbers.
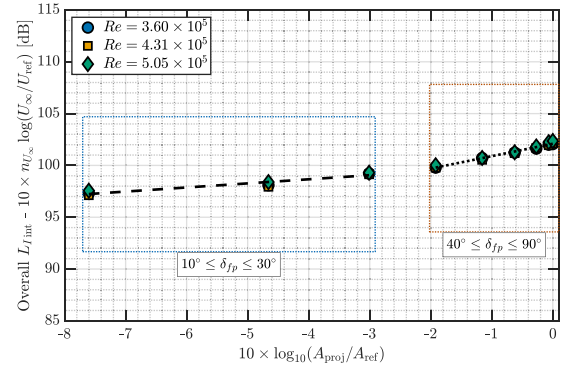
(b) Projected area scaling for the overall integrated acoustic intensity normalised to a reference velocity, $U_{ref} = 60$ m/s ($Re = 4.31 \times 10^5$).

Fig. 13. Projected area scaling for overall integrated acoustic intensity.

Table 2
Projected area scaling exponent, n_A, over the entire frequency range as a function of Re number and δ_{fp}.

Re	$10° \leq \delta_{fp} \leq 30°$	$40° \leq \delta_{fp} \leq 90°$
3.6×10^5	0.3	1.2
4.3×10^5	0.4	1.2
5.1×10^5	0.5	1.2

determined previously, it is more complicated than a simple dipole scaling law.

In contrast, at lower deflection angles ($\delta_{fp} \leq 30°$), the scaling exponent reduces significantly to approximately 0.4 at $U_\infty = 60$ m/s. This deviation from dipole-like scaling is due to more of the plate being immersed in the boundary layer compared to when it is at higher deflection angles. This changes the scaling with respect to the projected area and explains why there was only a relatively weak dependency on projected area at low deflection angles. The evidence that the lowest flat plate deflection angles are influenced by being immersed in the boundary layer is also shown in the scaling exponent data in Table 2 for different Reynolds numbers. At deflection angles above 40° the scaling exponent with projected area is 1.2 and does not change with Reynolds number. Conversely, at low deflection angles, where the height of the boundary layer relative to the projected height of the plate is greater, the scaling exponent varies much more. The boundary layer is a function of the Reynolds number and therefore is expected to have a greater effect on the low deflection angles. This difference in behaviour between low and high deflection angles was also seen in the aerodynamic force data, where the normalized normal force coefficient, C_N^*, (shown in Fig. 9(b)) approached a limiting value at high deflection angles, but deviated significantly from this limiting value at deflection angles less than 30°.

To see how the velocity normalized data scaled, Fig. 13(b) shows the overall $L_{I\,\text{int}}$ values normalized by velocity using the scaling law values previously determined and referenced to $U_{\text{ref}} = 60$ m/s (equivalent to $Re = 4.31 \times 10^5$). The velocity scaling exponent, n_{U_∞}, was varied for each deflection angle, using the values tabulated in Table 1. The results demonstrate a good collapse of the three datasets, confirming the two distinct scaling relationships observed in Fig. 13(a). Linear regression analysis, over the two defined angle ranges, reveals that for higher deflection angles ($40° \leq \delta_{fp} \leq 90°$), $n_A \approx 1.2$, consistent with values obtained for scaling at each individual Reynolds number. For smaller deflection angles ($10° \leq \delta_{fp} \leq 30°$), the collapse is not as good, due to the Reynolds number dependencies in this angle regime previously discussed. The value was $n_A \approx 0.4$, which lies in the mid range of the values previously presented in Table 2 for each Reynolds numbers.

5. Conclusions

This work investigated scaling laws for the aerodynamic loads and aeroacoustic noise of wall-mounted inclined flat plates for different deflection angles ranging from 10° to 90°. The experiments were conducted in a hybrid Kevlar-walled test section, which offered significant advantages over traditional open-jet configurations for acoustic measurements by constraining the wake expansion downstream of the flat plate and reducing background noise due to the interaction of the wake with the collector in an open test section wind tunnel, and increasing the signal-to-noise ratio. This was particularly important at high flat plate deflection angles.

While advantageous for acoustic measurements, the use of a Kevlar test section necessitated aerodynamic corrections for solid body and wake blockage effects. A procedure based on a correction method for lifting wings in a Kevlar test section was extended for bluff body flows. It differed in two key aspects. The first is that the correction was based on the bluff body blockage corrections of Maskell. The second was that the porosity factor was calculated by optimizing agreement with experimental open jet data where blockage effects were negligible. The optimum value of this porosity factor, determined experimentally, was $\Omega = 0.45$ for the inclined plate at a deflection of $\delta_{fp} = 90°$. This is consistent with previous findings in literature for lifting wings in Kevlar test sections.

The normalized normal force coefficient exhibits a good collapse when scaled with the projected frontal area. For deflection angles above 50°, the normalized normal force coefficient converges to a value equal to the drag coefficient of the plate at a deflection angle of 90°. For deflection angles below $\delta_{fp} = 30°$, a slightly worse agreement was observed. However, due to the wall-mounted flow topology, the downforce generated at these angles is smaller than that generated in freestream, resulting in only small variations from the maximum value at $\delta_{fp} = 90°$. This scaling behaviour applies to flat plates where the pressure forces dominate. It provides a simple predictive method requiring only knowledge of the normal drag coefficient at $\delta_{fp} = 90°$. Due to the difference in the lift mechanism generated between plates in freestream and wall-mounted plates, this scaling relationship does not apply to plates in freestream. The defined scaling relationship demonstrated good agreement between the measured and predicted aerodynamic loads, with maximum absolute errors of $\Delta C_D \leq 0.073$ and $\Delta C_L \leq 0.081$ across the deflection angle range.

The analysis of the flow-induced noise by an inclined wall-mounted flat plate revealed a non-trivial scaling relationship, which suggests a more complex noise generation which varies across different deflection angles and frequency ranges. The noise generated by a wall-mounted flat plate is broadband in nature without distinct low-frequency peaks corresponding to coherent bluff body vortex shedding. The radiated noise scales approximately but not perfectly with the sixth power of velocity, consistent with dipole characteristics. However, the exact velocity exponent varied with the deflection angle. At lower deflection angles ($\delta_{fp} \leq 20°$), the exponent was less than six, indicating a

Table A.1

Microphone locations with respect to the model axis shown in Fig. 3.

Microphone	x (m)	y (m)	z (m)
1	−0.602	−0.21	1.343
2	−0.452	−0.21	1.341
3	−0.302	−0.21	1.339
4	−0.152	−0.21	1.337
5	−0.002	−0.21	1.335
6	0.148	−0.21	1.333
7	0.298	−0.21	1.331
8	−0.413	0	1.344
9	0	0	1.337
10	0.305	0	1.333

mixture of dipole and edge scattering sources. At higher deflection angles ($\delta_{fp} \geq 30°$), slightly higher velocity exponents were observed, consistent with other findings in the literature for wall-mounted square obstacles partially immersed in a turbulent boundary layer.

Projected area scaling for the noise revealed two distinct scaling relationships corresponding to low ($10° \leq \delta_{fp} \leq 30°$) and high ($40° \leq \delta_{fp} \leq 90°$) deflection angles. For the overall frequency range, the integrated acoustic intensity at higher deflection angles scaled with an exponent approximately equal to 1.2. While this is close to the theoretical dipole scaling value of unity, it exceeds it, indicting a more complex scaling relationship. Previous work has identified the acoustic sources for a wall-mounted flat plate to be associated with the broadband bluff body wake, the horseshoe vortex, as well as the ground edge vortices and the flat plate side-edges. These sources do not scale simply with the projected area of the flat plate. At lower deflection angle, the exponent reduced significantly to 0.4, with variations across different Reynolds numbers as a greater proportion of the flat plate was immersed in the boundary layer.

CRediT authorship contribution statement

Owen Parnis: Writing – original draft, Visualization, Validation, Software, Methodology, Investigation, Formal analysis, Data curation, Conceptualization. **David Angland:** Writing – review & editing, Supervision, Project administration, Funding acquisition, Formal analysis, Conceptualization.

Declaration of competing interest

The authors declare that they have no known competing financial interests or personal relationships that could have appeared to influence the work reported in this paper.

Acknowledgements

Appendix. Microphone location

See Table A.1

Data availability

Data published in this paper are available from the University of Southampton repository at https://doi.org/10.5258/SOTON/D3688.

References

Abernathy, F.H., 1962. Flow over an inclined plate. J. Fluid Eng. Transect. ASME 84 (3), 380–388. http://dx.doi.org/10.1115/1.3657331.

Agui, J., Andreopoulos, J., 1990. Experimental investigation of a three dimensional boundary layer flow in the vicinity of an upright wall mounted cylinder. In: 21st Fluid Dynamics, Plasma Dynamics and Lasers Conference.

Allen, H., Vincenti, W., 1944. Wall Interference in a Two-Dimensional-Flow Wind Tunnel, with Consideration of the Effect of Compressibility. Technical Report NACA-TR-3423, NACA.

Aly, A., Bitsuamlak, G., 2013. Aerodynamics of ground-mounted solar panels: Test model scale effects. J. Wind Eng. Ind. Aerodyn. 123, 250–260. http://dx.doi.org/10.1016/j.jweia.2013.07.007.

ATI Industrial Automation, 2021. Six-axis force/torque sensor system. Installation and Operation Manual.

Becker, S., Hahn, C., Kaltenbacher, M., Lerch, R., 2008. Flow-induced sound of wall-mounted cylinders with different geometries. AIAA J. 46 (9), 2265–2281. http://dx.doi.org/10.2514/1.34865.

Becker, S., Lienhart, H., Durast, F., 2002. Flow around three-dimensional obstacles in boundary layers. J. Wind Eng. Ind. Aerodyn. 90, 265–279. http://dx.doi.org/10.1016/S0167-6105(01)00209-4.

Capone, A., Romano, G., 2019. Investigation on the effect of horizontal and vertical deflectors on the near-wake of a square-back car model. J. Wind. Eng. Ind. Aerodyn. 185, 57–64. http://dx.doi.org/10.1016/j.jweia.2018.12.011.

Chen, J., Feng, Y., 1996. Strouhal numbers of inclined flat plates. J. Wind Eng. Ind. Aerodyn. 61, 99–112. http://dx.doi.org/10.1016/0167-6105(96)00044-X.

Curle, N., 1955. The influence of solid boundaries upon aerodynamic sound. Proc. R. Soc. Lond. Ser. A. Math. Phys. Sci. 231 (1187), 505–514. http://dx.doi.org/10.1098/rspa.1955.0191.

Devenport, W., Burdisso, R., Borgoltz, A., Ravetta, P., Barone, M., 2010. Aerodynamic and acoustic corrections for a kevlar-walled anechoic wind tunnel. In: 16th AIAA/CEAS Aeroacoustics Conference. http://dx.doi.org/10.2514/6.2010-3749.

Devenport, W., Burdisso, R., Borgoltz, A., Ravetta, P., Barone, M., Brown, K., Morton, M., 2013. The kevlar-walled anechoic wind tunnel. J. Sound Vib. 332, 3971–3991. http://dx.doi.org/10.1016/j.jsv.2013.02.043.

Everitt, K.W., 1982. Normal flat plate close to a large plane surface. Aeronaut. Q. 33 (pt 1), 90–104. http://dx.doi.org/10.1017/s0001925900009318.

Ewald, B. (Ed.), 1998. Wind Tunnel Wall Correction. In: AGARD Advisory Group for Aerospace Research and Development, RTO/NATO, no. 336, RTO/NATO, AGARD-AG-336.

Fage, A., Johansen, F., 1927. On the flow of air behind an inclined flat plate of infinite span. Proc. R. Soc. Lond. Ser. A. Mathematical Phys. Sci. 147 (1876), 170–197.

Fail, R., Lawford, J., Eyre, R., 1959. Low-speed-experiments on the wake characteristics of flat plates normal to an air stream. Aeronaut. Res. Counc. Rep. Memo. 310.

Fail, R., Owen, T., Eyre, R., 1956. Preliminary Low Speed Wind Tests on Flat Plates and Air Brakes. Technical Report, URL: http://reports.aerade.cranfield.ac.uk/handle/1826.2/264.

Flachsbart, O., 1932. Messungen an ebenen und gewölbten platten. Ergeb. AVA IV.

Gutierrez-Castillo, P., Aguilar-Cabello, J., Alcalde-Morales, S., Parras, L., del Pino, C., 2021. On the lift curve slope for rectangular flat plate wings at moderate Reynolds number. J. Wind. Eng. Ind. Aerodyn. 208, 104459. http://dx.doi.org/10.1016/j.jweia.2020.104459.

Hackett, J., 1996. Tunnel induced gradients and their effect on drag. AIAA J. 2575–2581. http://dx.doi.org/10.2514/3.13441.

Hemmati, A., Wood, D., Martinuzzi, R., 2018. On simulating the flow past a normal thin flat plate. J. Wind Eng. Ind. Aerodyn. 174, 170–187. http://dx.doi.org/10.1016/j.jweia.2017.12.026.

Hoerner, S., 1965. Fluid-Dynamic Drag: Practical Information on Aerodynamic Drag and Hydrodynamic Resistance, first ed. Hoerner, S.F, New Jersey.

Holmes, J., Letchford, C., Lin, N., 2005. Investigations of plate-type windborne debris - part II: Computed trajectories. J. Wind Eng. Ind. Aerodyn. 94, 21–39. http://dx.doi.org/10.1016/j.jweia.2005.10.002.

Howe, M., 2003. Theory of Vortex Sound, first ed. Cambridge University Press.

Ivanova, Z., Angland, D., 2022. Southampton anechoic wind tunnel (sotonawt) aerodynamic and acoustic characterisation. In: 28th AIAA/CEAS Aeroacoustics Conference. http://dx.doi.org/10.2514/6.2022-2854.

JCGM, 2008. Evaluation of measurement data — guide to the expression of uncertainty in measurement, first ed. JCGM, Sèvres, France, corrected version 2010, URL: http://www.bipm.org/en/committees/jc/jcgm.

Joppa, R., 1973. Wind tunnel interference factors for high-lift wings in closed wind tunnels. Nasa Contractor Report, NASA CR-2191.

King, W.F., Pfizenmaier, E., 2009. An experimental study of sound generated by flows around cylinders of different cross-section. J. Sound Vib. 328 (3), 318–337. http://dx.doi.org/10.1016/j.jsv.2009.07.034.

Maruta, Y., Kanagawa, F., 1981. Separated flow noise of a flat plate at large attack angles. In: AIAA 7th Aeroacoustic Conference. http://dx.doi.org/10.2514/6.1981-2050.

Maskell, E., 1963. A theory of the blockage effects on bluff bodies and stalled wings in a closed wind tunnel. URL: https://reports.aerade.cranfield.ac.uk/handle/1826.2/3982.

Mizoguchi, M., Yamaguchi, Y., 2012. Aerodynamic characteristics of rectangular flat plate wings in low Reynolds number flows. J. Japan Soc. Aeronaut. Space Sci. 60 (3), 121–127, (in Japanese) with English abstract.

Montes Gomez, E., Sumner, D., 2022. The wake of a rectangular flat plate. Fluid Dynamic Research 54, http://dx.doi.org/10.1088/1873-7005/acabe3.

Moreau, D.J., Doolan, C.J., 2013. Flow-induced sound of wall-mounted finite length cylinders. AIAA J. 51 (10), 2493–2502. http://dx.doi.org/10.2514/1.J052391.

Ortiz, X., Rival, D., Wood, D., 2015. Forces and moments on flat plates of small aspect ratio with application to PV wind loads and small wind turbine blades. Energies 8 (4), 2438–2453. http://dx.doi.org/10.3390/en8042438.

Parnis, O., Angland, D., 2025. Numerical simulation of the aerodynamics and acoustic of a wall-mounted spoiler. AIAA J. 63 (9), 3493–4009. http://dx.doi.org/10.2514/1.J064906.

Pelletier, A., Mueller, T.J., 2000. Low Reynolds number aerodynamics of low-aspect-ratio, thin/flat/cambered-plate wings. J. Aircr. 37 (5), 825–832. http://dx.doi.org/10.2514/2.2676.

Phillips, O., 1956. The intnesity of aeolian tones. J. Fluid Mech.

Pieris, S., Yarusevych, S., Peterson, S., 2022. Flow development over inclined flat plates in ground effect and relation to aerodynamic loads. Phys. Fluids 34 (9), http://dx.doi.org/10.1063/5.0102406.

Porteous, R., Doolan, C.J., Moreau, D.J., 2013. Directivity pattern of flow-induced noise from a wall-mounted, finite length circular cylinder. In: Proceedings of Acoustics. Victoria Harbor.

Porteous, R., Moreau, D.J., Doolan, C.J., 2014. A review of flow-induced noise from finite wall-mounted cylinders. J. Fluids Struct. 51, 240–254. http://dx.doi.org/10.1016/j.jfluidstructs.2014.08.012.

Strobel, K., Banks, D., 2014. Effects of vortex shedding in arrays of long inclined flat plates and ramifications for ground-mounted photovoltaic arrays. J. Wind Eng. Ind. Aerodyn. 133, 146–149. http://dx.doi.org/10.1016/j.jweia.2014.06.013.

Sundeep, S., Bu, H., Zhong, Z., Zhang, X., 2022. An experimental study of aerodynamic noise from large obstructions in turbulent boundary layer flows. Phys. Fluids 34, http://dx.doi.org/10.1063/5.0080426.

Taira, K., Colonius, T., 2009. Three-dimensional flows around low-aspect-ratio flat-plates wings at low Reynolds numbers. J. Fluid Mech. 623, 187–207. http://dx.doi.org/10.1017/S0022112008005314.

Torres, G., Mueller, T., 2004. Low-aspect-ratio wing aerodynamics at low Reynolds numbers. AIAA J. 42 (5), 865–873. http://dx.doi.org/10.2514/1.439.

Wang, Y., Thompson, D., Hu, Z., 2019. Effects of aspect ratio on flow and noise from cuboids. In: 25th AIAA/CEAS Aeroacoustics Conference, 2019. http://dx.doi.org/10.2514/6.2019-2671.

Wick, B., 1954. Study of the Subsonic Forces and Moments on an Inclined Plate of Infinite Span. Technical Report, National Advisory Comittee for Aeronautics, pp. 1–25.